Modelling of Quantum Transport in Weakly coupled Quantum Dots: An emphasis On Graphene
DDP Report Phase 1

Anuranan Das
Guide: Prof. Bhaskaran Muralidharan

October 18, 2022

Contents

Quantum technologies have emerged as a prospective alternative to conventional electronics in the post-Moore era. Many platforms are being explored to be set up as hosts for computational quantum bits or qubits. Graphene is one of the most suited candidates for hosting such qubits. Recently, qubits in graphene have been realized regarding two degrees of freedom associated with the system: spin and valleys. Although several experimental works have seen the light of day, compact theoretical modeling of transport-mediated characteristics in these systems is yet to be introduced. In this project, our focus is to explore the possibilities of employing already established quantum transport theory to develop a simulable model to explain and predict the behavior of a similar class of systems.

1 Prior Works

Entanglement Generation in spin coupled Quantum dots: I worked on a solid-state thermal machine to generate entanglement between two distant spins. The idea was to control the steady state currents of the system by applying and manipulating specific dc voltages. We analyzed the system's Liouvillian to find the final stable states. The composite Hamiltonian of the system is defined by

$$H = H_{\mathrm{D}} + H_{\mathrm{C}} + H_{\mathrm{A}} + H_{\mathrm{DC}} + H_{\mathrm{DA}}$$

where $H_{\mathrm{D}}, H_{\mathrm{C}}$ and H_{A} represent the Hamiltonians of the dot, contacts and ancillae respectively. The term H_{DC} is the tunneling Hamiltonian between the dot and contacts, and H_{DA} signifies the exchange coupling between the ancillae and the dot. The dot consists of two spin-degenerate energy levels at ϵ and with Coulomb interaction U.

The schematic of the device is included in fig. 1. Our analysis for the transport setup followed the approach by *Braig et al.*[1]. We assume that the strength of contact-to-dot electron coupling is smaller than the contact-induced thermal broadening of the energy levels in the dot. The dynamics of an open quantum system are given by the master equation of Lindblad form, written canonically as

$$\dot{\rho} = -\mathrm{i}[H, \rho] + \sum_k \gamma_k \mathcal{D}\left[O_k\right] \rho$$

We can infer an open system evolution's transient and steady-state dynamics from the eigenspectra of the Liouville superoperator. Such a Liouville superoperator vectorizes the dynamics to Liouville–Schmidt space, given by the form

$$|\dot{\rho}\rangle = \mathcal{L}|\rho\rangle$$

Entanglement generation is an important problem for quantum technologies. In the context of quantum dot systems, such entanglement generation can be between quantum dots or in impurity atoms interacting with the quantum dots. The work details can be found at [2].

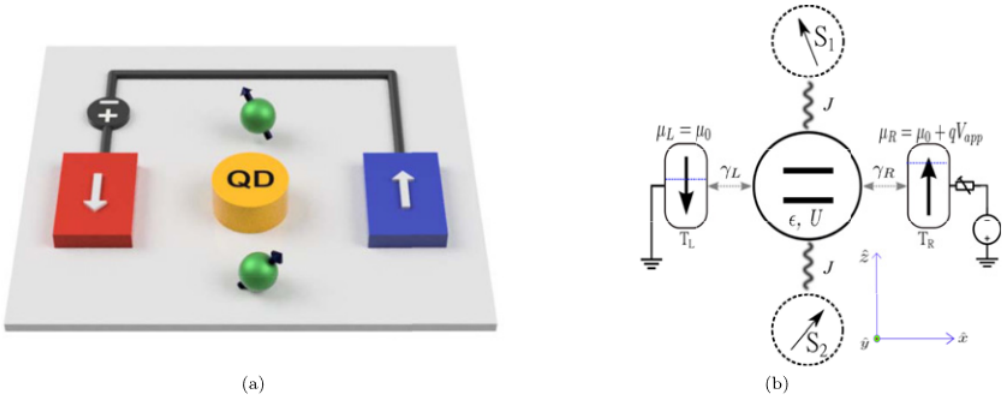

Figure 1: Figure 1. Schematic of the voltage-controlled steady state entanglement switch device: (a) the device consists of a quantum dot (shown in yellow) weakly coupled to spin-polarized contacts (red and blue boxes) and placed in a bath of two spin 1/2 impurities (green spheres) with which it interacts strongly. Steady-state entanglement is generated between the two constituent impurity spins, which can be controlled by the voltage applied across the contacts. (b) The dot is coupled to oppositely spin-polarized left and right contacts with electronic transport rates γ_{L} and γ_{R} respectively. Interaction coupling between the impurity spins and the quantum dot is represented by J. The left contact is held at constant potential μ_{L} and a voltage bias $V_{\mathrm{app}} = (\mu_{\mathrm{R}} - \mu_{\mathrm{L}})/q$ is applied across the two contacts which are at temperatures T_{L} and T_{R} respectively. Dot onsite energy is represented by ϵ, and the charging energy is U. Interaction between the dot and bath is stronger than the electronic transport rates. Therefore, the complete dot-impurity system can evolve and pass through entangled states before the electron exits.

2 Spin Qubits

The spin-based platform has been considered an attractive candidate for solid-state qubits as they allow controlled coupling of one or more electrons, using rapidly switchable voltages applied to electrostatic gates. A variety of spin qubits has been reported and realized in semiconductor systems. A brief description of the significant types is given [3].

2.1 Loss-DiVincenzo (LD) spin qubit

Here the spin 1/2 configuration is naturally considered to work as a qubit. The encoding for a single electron spin 'Loss-DiVincenzo' qubit is a direct mapping $\mathbf{S}_i = \boldsymbol{\sigma}_i/2$. The Loss-DiVincenzo qubit requires a method of initialization and measurement of single electron spin states. In actual practice, spin-selective tunnelling to a Fermionic bath of electrons using a large magnetic field B enables tunnelling of the higher energy QD spin-state to the Fermi sea. The presence or absence of a tunnelling event, as measured using sensitive charge detectors, is then used to infer the orientation of the electron spin.

2.2 Donor spin qubits

Bruce Kane published a proposal to use the nuclear spins of ^{31}P donor atoms in silicon to construct a quantum computer. The donor electron has a hydrogenic s-like ground state with an effective Bohr radius of 1.8 nm. Measurement philosophy uses gate tuning of electronic wavefunctions. Since Kane's

proposal, many elements of this qubit type have been demonstrated, and in so doing, many critical variations on the donor-qubit concept have emerged.

2.3 Singlet-triplet (ST_0 and $ST_\pm$)qubits

The most straightforward extension of a single qubit is the one from a double quantum dot and originates from exchange interaction between singlet-triplet (ST_0) qubit. Along with the basis states, the encoded qubit Pauli operators σ^x, σ^y, and σ^z are defined such that the ± 1 eigenstates of σ^z are the encoded states and the 0-eigenstates are leakage state.
Pauli spin blockade, a manifestation of exchange coupling, enables straightforward, rapid, and high-fidelity measurement of joint spin states. A spin blockade measurement converts singlets and triplets to different spatial configurations of the two electrons in the DQD, which a nearby charge sensor can easily distinguish.

2.4 Exchange-only (EO) and resonant-exchange (RX) qubits

The LD qubits described in the first section require the following exchange interactions:

- An entangling spin-spin coupling, typically the exchange interaction, can be further used to realize two-qubit gates.
- An effective magnetic field to manipulate the up and down state cases by implementing single qubit gates.

However, it is possible to allow for universal quantum computation with the exchange interaction alone if employing qubits defined by an encoded subspace with constant total spin. These gates are operated by sequentially pulsing on and off the exchange coupling between a pair of disjoint spins.
The RX qubit differs from the dc-mode EO qubit in that the nearest-neighbor exchange couplings are constantly set to the same non-zero value instead of zero. Noise mitigation and other motives have led to further growth of these qubits in the form of asymmetric resonant-exchange(ARX) qubits and always-on exchange-only (AEON) qubits concepts.

2.5 Spin qubits with additional charge degrees of freedom

One can create qubit variants by putting multiple spins into common sites or correlating sites to spin, to more strongly exploit spin-charge hybridization for qubit initialization and readout, electric-field control, and electric-dipole coupling to other qubits or cavity electric fields.

3 Singlet-triplet spin qubit manipulation

Manipulation of singlet-triplet(ST) qubits can be achieved, and several findings have been reported on the same.[4] The relative energy detuning ϵ of the (0,2) and (1,1) charge states can be rapidly controlled by applying calibrated voltage pulses to gates L and R. The control cycle of the experiments mainly involves the following stages (refer fig. 2):

- **Preparation:** Quantum point contact (QPC) sensors fabricated next to each dot serve as a local electrometer and hence shows the signature of electron addition into the system. The transfers to a certain dot state are mediated by tunnel barriers controlled by voltages V_L and V_R(L, left; R, right) and they connect the dots to adjacent reservoirs, allowing electron transfer to the dots.

- **Singlet separation:** The detuning between the dots can be used to get the transition from (0,2) to (1,1) and vice versa. Tight confinement in (0,2) favors a spin-singlet configuration, denoted (0,2)S, for above a certain energy threshold. For values below the threshold (1,1), energy states are preferable. In this case, four spin states are accessible: the singlet(S00), denoted S [suppressing the (1,1) label]; and three triplets (S01), denoted $T_{-}, T_0, and T_{+}$, corresponding to $m_s = -1, 0, +1$. In absence of magnetic field effects, these states are degenerate.
- **Evolution:** Spin manipulation after preparation and separation can be done by a number of techniques, namely,
  - Spin SWAP and Rabi Oscillation-based manipulation.
  - Singlet-triplet spin-echo-based occurrences.
- **Measurement:** In all measurements, a cyclical pulse sequence can be used. The method involves projecting the state onto (0,2) state by QPC and selective tunnelling of (0,2) states.

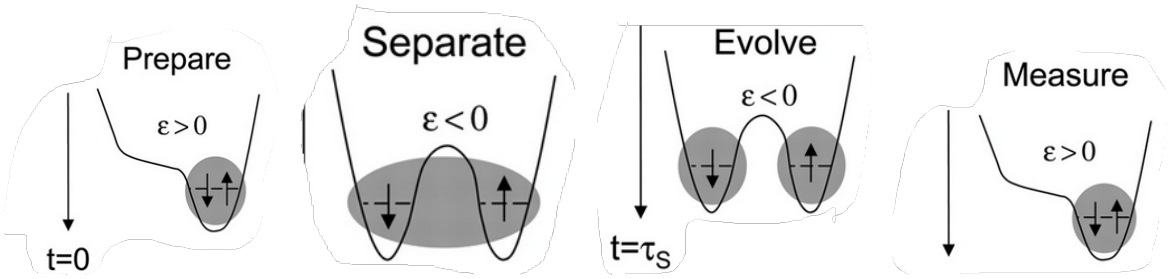

Figure 2: Spin Manipulation for S-T qubits.

4 Transport Formalism in Weakly Coupled Double QDs

4.1 The Hamiltonian

One can consider a double quantum dot, as shown in Fig. 3, that comprises two dots with spin degenerate orbitals. The DQD Hamiltonian[5] can be defined in a localized orbital basis as

$$\hat{H}_{\mathrm{DQD}} = \sum_{i\sigma} \varepsilon_i n_{i\sigma} - t \sum_{\sigma} \left(c^{\dagger}_{1\sigma} c_{2\sigma} + \text{ h.c. } \right) + U \sum_{i} n_{i\uparrow} n_{i\downarrow} + U_{nn} \sum_{\sigma\sigma'} n_{1\sigma} n_{2\sigma'} \tag{1}$$

with on-site energy ε_i and inter-dot hopping t. $c^{\dagger}_{i\sigma}, c_{i\sigma}$ are Fermi operators for the molecular levels, and $n_{i\sigma} = c^{\dagger}_{i\sigma} c_{i\sigma}$ is the number operator. The strength of the intra-dot and inter-dot Coulomb repulsion is given by U and U_{nn} respectively.

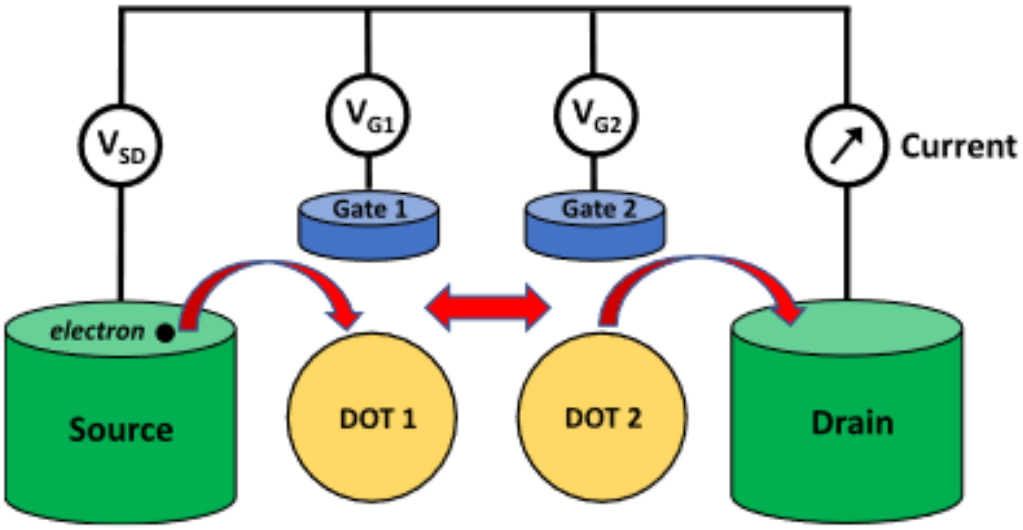

Figure 3: Toy Model for a Double Quantum Dot coupled to leads. [6]

4.2 Fermi's Golden Rule

The coherence factors can be calculated between two different states of the diagonalized hamiltonian using fermi's golden rule given by the following equation

$$\gamma_{ij}^{\alpha} = \gamma^{\alpha} \left| \left\langle N, i \left| c_m^{\dagger} \right| N-1, j \right\rangle \right|^2, \tag{2}$$

where $c_m^{\dagger}$ is the creation and/or annihilation operators for an electronic state on the end dot coupled with the corresponding electrode, and γ^{α} is the bare left or right electrode coupling factor.

4.3 Master Equations

Rate matrix-based master equations govern the transport in this system approach because the broadening is negligible. The total transition rates $W_{\chi,\chi'}^{(1)}$ (in the absence of relaxation) are the sum of the transition rates associated with electron tunnelling through either the left or the right barrier, $W_{\chi,\chi'}^{(1)} = W_{\chi,\chi'}^{(1)\mathrm{R}} + W_{\chi,\chi'}^{(1)\mathrm{L}}$ where χ and χ' are the many-body states. [7, 5]
Together with $\Gamma_r^{i\sigma} = 2\pi \left| t_{i\sigma}^r \right|^2 \rho_e$ we find

$$W_{\chi',\chi}^{(1)r} = 2\pi\rho_e \sum_{\sigma} \left[f_r^{+}\left(E_{\chi',\chi}\right) \left| \sum_i t_{i\sigma}^r \left\langle \chi' \left| c_{i\sigma}^{\dagger} \right| \chi \right\rangle \right|^2 + f_r^{-}\left(-E_{\chi',\chi}\right) \left| \sum_i t_{i\sigma}^r \left\langle \chi' \left| c_{i\sigma} \right| \chi \right\rangle \right|^2 \right] \tag{3}$$

for $\chi' \neq \chi$, together with $W_{\chi,\chi}^{(1)r} = -\sum_{\chi' \neq \chi} W_{\chi',\chi}^{(1)r}$ (sum rule). $E_{\chi',\chi} = E_{\chi'} - E_{\chi}$ is the energy difference between the many-body states χ and χ'. Here, $f(x) = 1/\left(\exp\left(x/k_{\mathrm{B}}T\right) + 1\right)$ is the Fermi function, $f^{+}(x) = f(x)$ and $f^{-}(x) = 1 - f(x)$, and $f_r^{\pm}(x) = f^{\pm}\left(x - \mu_r\right)$.

4.4 Inelastic Processes - Photon Relaxation

Photon relaxation processes, as illustrated in fig. 4 can be included in the sense that electrons on the dot can change the level by emitting or absorbing a photon for $i \neq j$ with the Hamiltonian

$$H_{\rm ph} = H_B + H_{B-D} = \sum_q \omega_q d_q^\dagger d_q + \sum_{q\sigma ij} g_{ph}\left(d_q^\dagger + d_q\right) c_{i\sigma}^\dagger c_{j\sigma} \tag{4}$$

where we consider the coupling amplitudes to be independent of i, j and q.

Assuming weak coupling to the bosonic bath (in addition to weak tunneling), we only keep contributions to either first order in α_{ph}. The total transition rates are, thus, given by

$$W^{(1)}_{\chi,\gamma'} = W^{(1)\rm l}_{\chi,\chi'} + W^{(1)\rm r}_{\chi,\chi'} + W^{(1)ph}_{\chi,\chi'}. \tag{5}$$

The bosonic rates are

$$W^{(1)\rm ph}_{\chi',\chi} = \sum_\sigma b\left(E_{\chi',\chi}\right) \left| \sum_{i\neq j} \left\langle \chi' \left| c_{i\sigma}^\dagger c_{j\sigma} \right| \chi \right\rangle \right|^2 \tag{6}$$

for $\chi' \neq \chi$, and $W^{(1)\rm ph}_{\chi,\chi} = -\sum_{\chi'\neq\chi} W^{(1)\rm ph}_{\chi',\chi}$, where $b(x) = {\rm sign}(x)\alpha_{\rm ph}(x)n_{\rm b}(x)$, with the Bose function $n_{\rm b}(x) = 1/\left(\exp\left(x/k_{\rm B}T\right) - 1\right)$. This allows us to build the matrix block $\mathbf{W^{(1)}}$ and find out probabilities to get the current through the dots using the below stationary master equation and current expression.

$$\mathbf{W^{(1)}p}^{\rm st} = 0 \tag{7}$$

$$I = \frac{e}{2\hbar}\mathbf{e}^T\mathbf{W^{(1)r}p}^{\rm st} \tag{8}$$

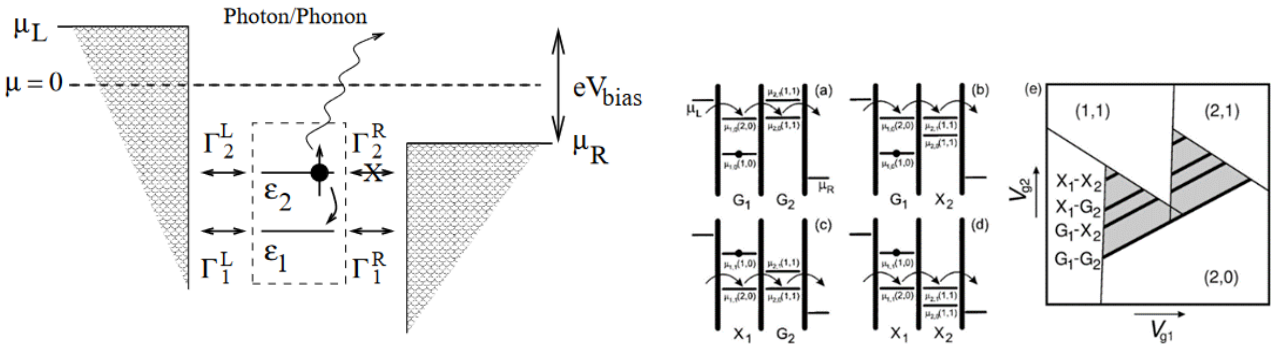

Figure 4: (a) Schematic of boson-based relaxation in a single QD. (b) The origin of triangles in the high bias regime, the grey triangle, corresponds to inelastic tunneling, while dark lines correspond to resonant tunneling effects. [3, 8]

5 Logic For Transport Codes

Codes were constructed in MATLAB. The program flow consisted of the following :

- Define constants and arrays for varying parameters of Interest
- Formulate diagonal and off-diagonal terminals using binary logic for each possible electron occupancy level.

- Compartmentalize the TBH into occupation number-based subspaces.
- Diagonalize each subspace and find out the many body eigenstates.
- Calculate gammas for sequential tunneling as well as relaxation processes.
- Formulated the Rate matrix in this same eigenstate basis and find the stationary probabilities and current.
- To look at occupancy in each dot, we need to revert back to the original basis in which the hamiltonian was written and then calculate expectation.

6 Results and Discussion

This section discusses the results and corresponding inferences from the work done up until now.

6.1 Coloumb blockade and NDR in DQDs

As an initial exercise, at the onset of the project, we reproduced the current-voltage characteristics in a double quantum dot from ref [5]. There were three cases described in detail in the relevant paper,

- Regular Coulomb-blockade plateaus in the absence of orbital offset since the Negative Differential Resistance (NDR) condition is not satisfied.
- Forward bias NDR, which occurs under certain conditions as derived.
- Reverse bias NDR can also occur in the presence of finite orbital offset with off-resonance.

The plots in fig. 5 are hereby depicted with a description of the conditions required to get them.

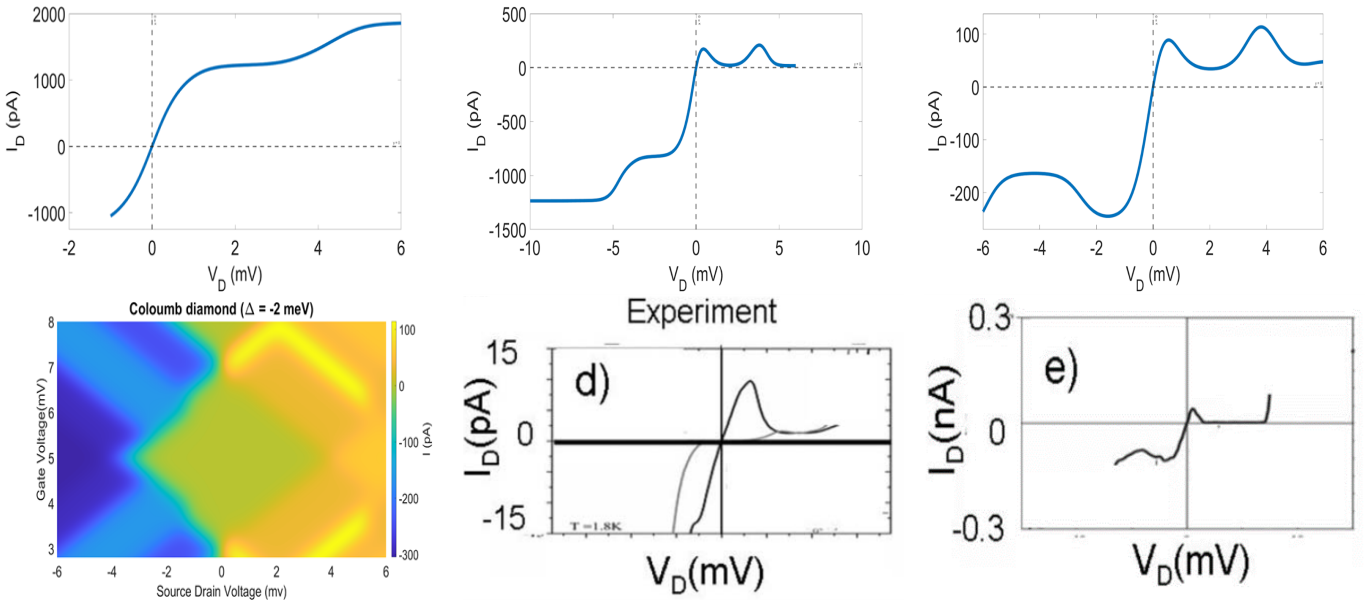

Figure 5: Reproduced diagrams from [5]. (a) A simulated case when there is no NDR with $\Delta\epsilon = 0, U_{11} = U_{22}$, (b) Simulated forward bias NDR with $\Delta\epsilon > 0$ with resonance $\epsilon_1 + U_{12} = \epsilon_2 + U_{22}$, (c) Simulated case for both forward and reverse NDR:: $\epsilon_1 + U_{12} < \epsilon_2 + U_{22}$, (d) Columb diamond on varying overall gate voltage with constant detuning versus the bias voltage, (e) Experimental forward bias NDR, (f) Experimental forward and reverse NDR.

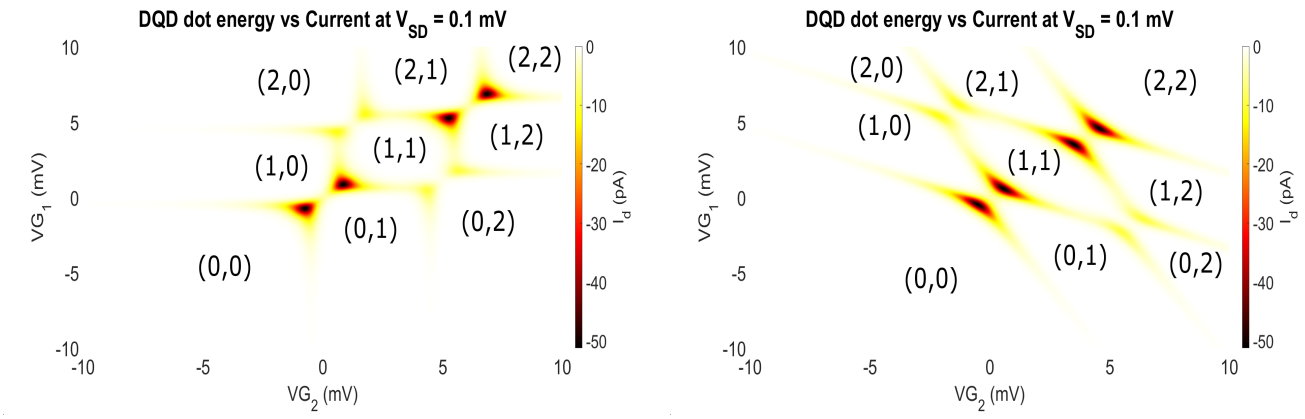

Figure 6: Charge Stability Diagrams for low bias of $V_{SD} = 0.1mV$. (a) No cross-capacitance coupling leads to a perfect honeycomb structure. Gate voltages are varied to tune each dot. The numbers mark the electron occupation number in each compartment. (b) Simulated with the cross-capacitance coupling of $\alpha_{ij} = 0.5$, signifying the effect of one dot on the other.

6.2 Charge Stability Diagram for two-level DQD

Charge stability diagrams are the signature of number-wise electron addition and removal in these systems and have been extensively realized in experiments. Classical models based on electrostatic capacitance have been extensively used to simulate the variation of the current characteristic with variable gate voltages. However, as discussed earlier, the Quantum mechanical approach is more robust and accurate in predicting the behavior of electrons in this system. Simulated current-voltage characteristics as shown in fig. 6 matches with experimentally obtained graphs.

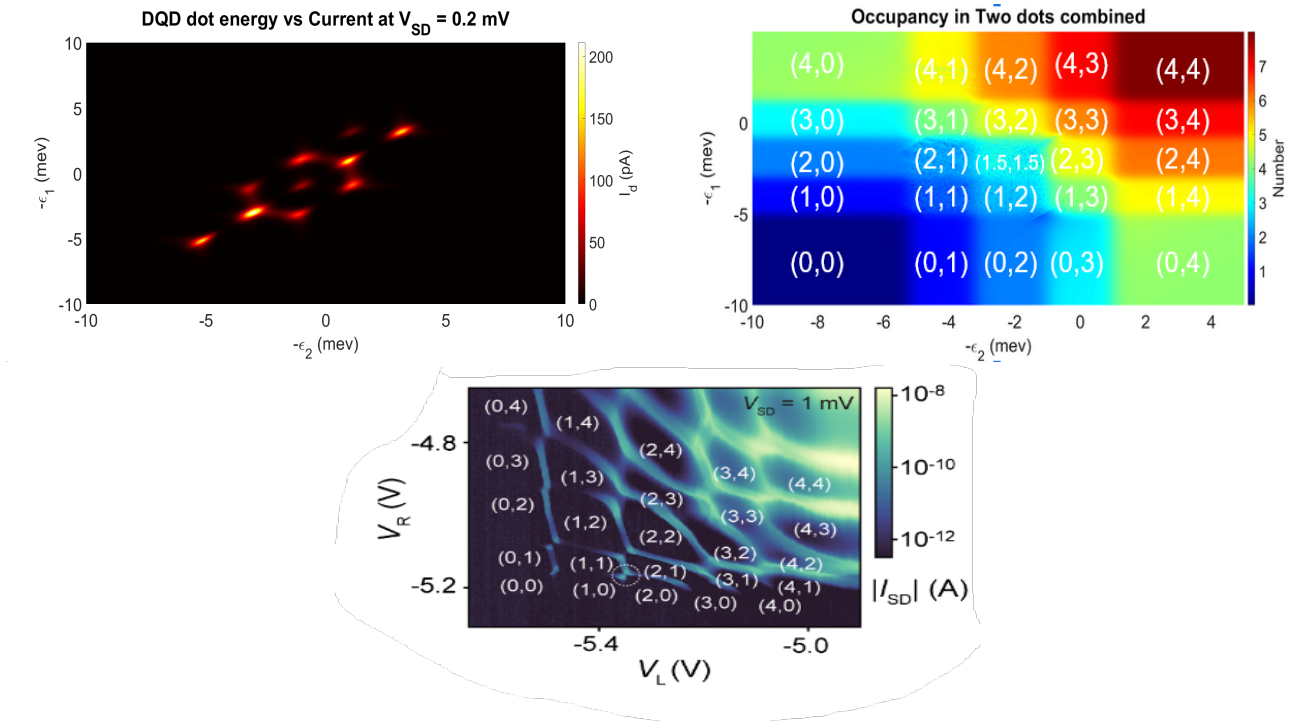

Figure 7: Charge Stability Diagrams of 4 level system for low bias of $V_{SD} = 200\mu V$. (a)Current as a function of gate voltages at a constant V_{SD}. The numbers mark the electron occupation number in each compartment. (b) Mapped Occupation levels for the 4 levels (c) Experimental Charge stability diagram from a Bilayer Graphene system.[9]

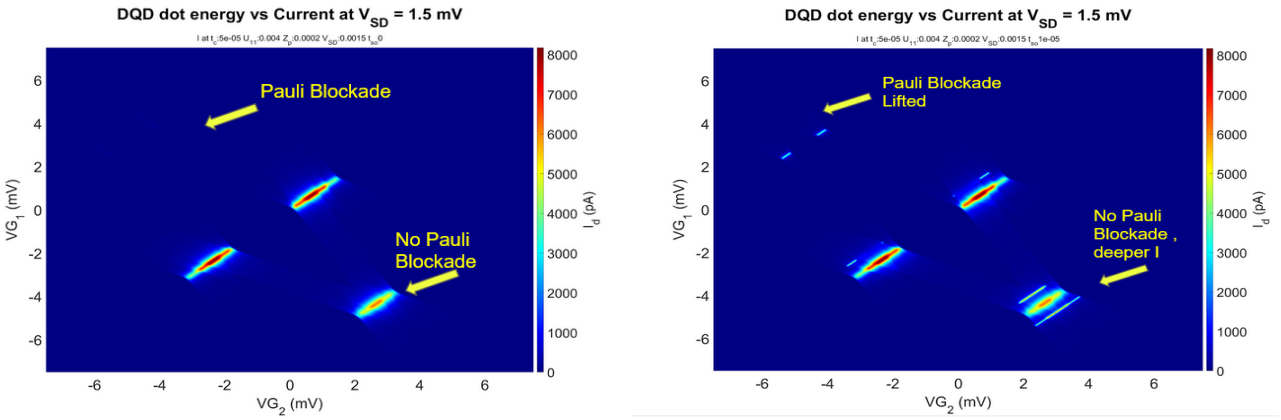

Figure 8: Effect of SO-coupling for low bias of $V_{SD} = 1.5mV$. (a)The charge stability diagram shows zero conductance at certain bias voltages, the signature of PSB. (b) PSB is lifted in these systems owing to the magnetic field application, and spin-orbit coupling with other parameters is kept constant.

6.3 Four-level Charge Stability Diagrams

The above system can be expanded to cases where we have 2 levels per dot; hence at maximum, 8 electrons can reside in the system. Figure 7 shows the relevant simulation outcomes and their match with experiments.

6.4 Addition of Spin-Orbit Coupling:

We revert back to the two-level system and describe the effects of spin-orbit coupling in them. If a certain magnetic field is added, then a non-zero SO coupling can result in spin-flip and conduction, leading to the lifting of Pauli Spin Blockade(PSB)[10]. This phenomenon has been observed in experiments and is also shown to be true from the simulations (see fig. 8).

6.5 Inelastic Scattering

All the simulations in the last parts took into account only resonant sequential tunneling processes. However, in natural systems, inelastic processes and cotunneling play a crucial role in forming bias triangles at the high bias regime [3, 11, 9]. We added a photon relaxation model and successfully replicated the formation of bias triangles for the system under consideration. I also replicated photon relaxation coupling effects on the current graph from [7] to verify the validity of the model implementations. Figures 9 illustrate the impact of Photon relaxation, formation of bias triangles, and effects of spin-orbit coupling.

7 Future work

This work shall be continued in my DDP phase 2. The idea is to create a similar transport setup for valley qubits[12, 13, 14]. We then plan to use this model to create a CNN model in conjunction with the transport to identify the spin and valley blockade phenomenon automatically.

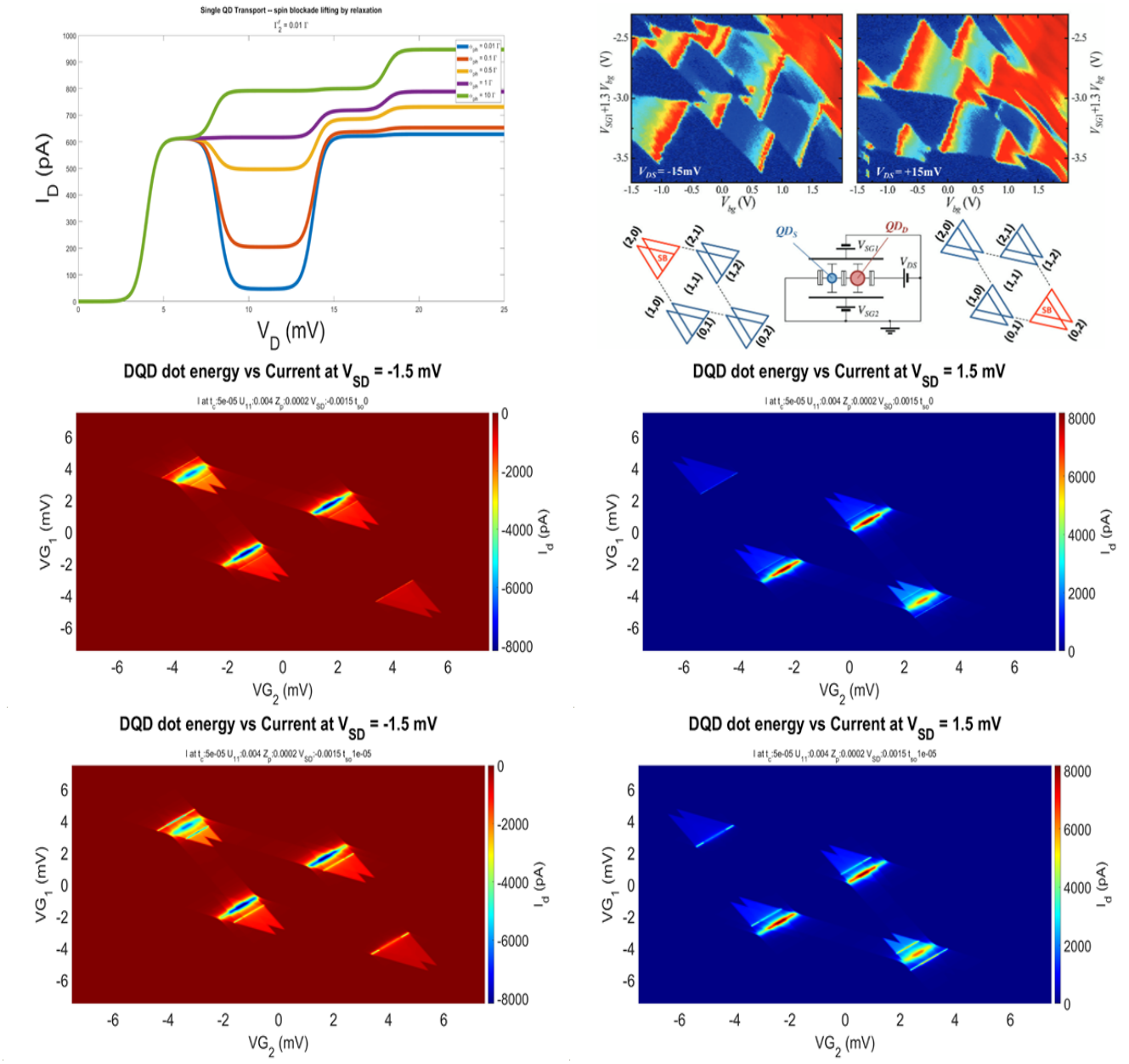

Figure 9: Effect of inelastic scattering processes. (a) Photonic relaxation processes lead to the lifting of the spin blockade in single quantum Dots. (b) Experimentally found bias triangles in a high bias regime.[9] (c) & (d) Simulated bias triangles without SO coupling at a high bias of $|V_{SD}| = 1.5mV$. Changing source drain voltage polarity changes the direction of bias triangles. (e) & (f) Adding spin-orbit coupling makes extra excited states available, giving rise to extra conduction lines as expected.

8 Acknowledgement

I am grateful for the careful and wise guidance of Prof. Bhaskaran and Dr. Bitan De in carrying out the research work. I am indebted to my classmate Adil Anwar Khan for his invaluable input on assistance with understanding the dynamics of the system.

References

[1] S. Braig and P. W. Brouwer, "Rate equations for coulomb blockade with ferromagnetic leads," *Phys. Rev. B*, vol. 71, p. 195324, May 2005. [Online]. Available: https://link.aps.org/doi/10.1103/PhysRevB.71.195324

[2] A. Das, A. A. Khan, S. D. Mishra, P. Solanki, B. De, B. Muralidharan, and S. Vinjanampathy, "Steady-state tunable entanglement thermal machine using quantum dots," 2021. [Online]. Available: https://arxiv.org/abs/2112.12020

[3] G. Burkard, T. D. Ladd, J. M. Nichol, A. Pan, and J. R. Petta, "Semiconductor spin qubits," 2021. [Online]. Available: https://arxiv.org/abs/2112.08863

[4] J. R. Petta, A. C. Johnson, J. M. Taylor, E. A. Laird, A. Yacoby, M. D. Lukin, C. M. Marcus, M. P. Hanson, and A. C. Gossard, "Coherent manipulation of coupled electron spins in semiconductor quantum dots," *Science*, vol. 309, no. 5744, pp. 2180–2184, 2005. [Online]. Available: https://www.science.org/doi/abs/10.1126/science.1116955

[5] B. Muralidharan and S. Datta, "Generic model for current collapse in spin-blockaded transport," *Phys. Rev. B*, vol. 76, p. 035432, Jul 2007. [Online]. Available: https://link.aps.org/doi/10.1103/PhysRevB.76.035432

[6] A. Rassekh, M. Shalchian, J.-M. Sallese, and F. Jazaeri, "Tunneling current through a double quantum dots system," *IEEE Access*, vol. 10, pp. 75 245–75 256, 2022.

[7] J. Aghassi, "Electronic transport and noise in quantum dot systems," 2007.

[8] W. G. van der Wiel, S. De Franceschi, J. M. Elzerman, T. Fujisawa, S. Tarucha, and L. P. Kouwenhoven, "Electron transport through double quantum dots," *Rev. Mod. Phys.*, vol. 75, pp. 1–22, Dec 2002. [Online]. Available: https://link.aps.org/doi/10.1103/RevModPhys.75.1

[9] F. Rossella, A. Bertoni, D. Ercolani, M. Rontani, L. Sorba, F. Beltram, and S. Roddaro, "Nanoscale spin rectifiers controlled by the stark effect," *Nature nanotechnology*, vol. 9, 11 2014.

[10] S. S. Kalantre, J. P. Zwolak, S. Ragole, X. Wu, N. M. Zimmerman, M. D. Stewart, and J. M. Taylor, "Machine learning techniques for state recognition and auto-tuning in quantum dots," *npj Quantum Information*, vol. 5, no. 1, p. 6, Jan 2019. [Online]. Available: https://doi.org/10.1038/s41534-018-0118-7

[11] T. Fujisawa, W. G. van der Wiel, and L. P. Kouwenhoven, "Inelastic tunneling in a double quantum dot coupled to a bosonic environment," *Physica E: Low-dimensional Systems and Nanostructures*, vol. 7, no. 3, pp. 413–419, 2000. [Online]. Available: https://www.sciencedirect.com/science/article/pii/S1386947799003525

[12] N. Rohling and G. Burkard, "Universal quantum computing with spin and valley states," *New Journal of Physics*, vol. 14, no. 8, p. 083008, aug 2012. [Online]. Available: https://doi.org/10.1088/1367-2630/14/8/083008

[13] M. Eich, F. c. v. Herman, R. Pisoni, H. Overweg, A. Kurzmann, Y. Lee, P. Rickhaus, K. Watanabe, T. Taniguchi, M. Sigrist, T. Ihn, and K. Ensslin, "Spin and valley states in gate-defined bilayer graphene quantum dots," *Phys. Rev. X*, vol. 8, p. 031023, Jul 2018. [Online]. Available: https://link.aps.org/doi/10.1103/PhysRevX.8.031023

[14] C. Tong, A. Kurzmann, R. Garreis, W. W. Huang, S. Jele, M. Eich, L. Ginzburg, C. Mittag, K. Watanabe, T. Taniguchi, K. Ensslin, and T. Ihn, "Pauli blockade of tunable two-electron spin and valley states in graphene quantum dots," 2021. [Online]. Available: https://arxiv.org/abs/2106.04722